

Effect of H₂S on CO₂ Corrosion of Mild Steel in HPHT Conditions

Yoon-Seok Choi, Fernando Farelas, Luciano Paolinelli, Srdjan Nesic
Institute for Corrosion and Multiphase Technology,
Department of Chemical and Biomolecular Engineering, Ohio University
342 West State Street
Athens, OH 45701
USA

Ahmad Zaki B Abas, Azmi Mohammed Nor, Muhammad Firdaus Suhor
Petronas Research SDN. BHD, Selangor Darul Ehsan, Malaysia

ABSTRACT

The effect of H₂S on the aqueous corrosion behavior of mild steel was evaluated at HPHT conditions (supercritical CO₂ pressure) at a total pressure of 12 MPa and a temperature of 160°C. The corrosion rate of steel samples was determined by electrochemical and weight loss measurements. The surface/cross-sectional morphology and the composition of the corrosion product layers were analyzed by using surface analytical techniques (SEM, EDS, and XRD). Results showed that the corrosion rate decreased with time and no significant difference was observed in the presence of 1000 and 2000 ppm of H₂S at HPHT CO₂ conditions. Surface and cross-sectional analyses revealed that the corrosion process is governed by the formation of FeCO₃ regardless of the presence of H₂S. Furthermore, the corrosion behavior of mild steel in these conditions did not depend significantly on flow velocity.

Key words: Supercritical CO₂, CO₂ corrosion, carbon steel, H₂S, high temperature

INTRODUCTION

The presence of large quantities of CO₂ (from 25% to 89%) in gas fields have imposed increased challenges on the economics of project development and subsequent operations.¹ A major issue in developing those fields is corrosion and materials technology because of aggressive environments (i.e., high CO₂ contents and/or presence of H₂S) with high pressures and high temperatures (HPHT).² Although corrosion resistance alloys (CRAs) have been available as a materials selection option for these severe environments, carbon and low alloy steels are still widely used as tubing materials due to their strength, availability and cost.³⁻⁷

The increment of temperatures and CO₂ pressure in production wells may lead to CO₂ in supercritical state if the temperature and the pressure are over 31.1°C and 7.38 MPa, respectively.⁸ Corrosion issues

in supercritical CO₂ environments relating to carbon capture and storage (CCS), enhanced oil recovery (EOR), and deepwater oil and gas production applications have recently been investigated at relatively low temperatures (< 90°C),⁹⁻¹³ and it has been understood that aqueous corrosion mechanisms in high pressure CO₂ are similar to those in low pressure CO₂ conditions.¹⁴

Regardless of the CO₂ pressure, there has been relatively less research on corrosion at high temperatures, above 100°C.^{15,16} In the temperature range from 90 ~ 250°C, general corrosion rates of carbon steel were shown to decrease with increasing temperature and were strongly dependent on the formation of magnetite (Fe₃O₄) because of the fast kinetics of Fe₃O₄ formation at high temperatures.^{17,18} This indicates that high temperature has a significant effect on the corrosion rate and formation/transformation of the corrosion products. Those effects were also shown in high temperature H₂S corrosion, yet the understanding of the associated corrosion mechanism is very limited.¹⁹⁻²¹

Until now, there are few studies for aqueous corrosion in high temperature supercritical CO₂ environments with H₂S related to the downhole conditions. Thus, the objective of the present study was to identify and quantify the key issues that affect the integrity of carbon steel in high temperature supercritical CO₂ in the presence of small amounts of H₂S.

EXPERIMENTAL PROCEDURE

The test specimens were machined from UNS K03014⁽¹⁾ carbon steel (CS) with two different geometries: cylindrical type with 5 cm² exposed area for electrochemical measurements, and rectangular type with a size of 1.27 cm × 1.27 cm × 0.254 cm for surface analysis. The chemical composition of the CS is shown in Table 1. The specimens were ground sequentially with 250, 400 and 600-grit silicon carbide paper, rinsed with deionized (DI) water, cleaned with isopropyl alcohol in an ultrasonic bath for 60 seconds, and then dried.

Table 1
Chemical compositions of materials used in the present study (wt.%, balance Fe).

	C	Cr	Mn	P	S	Si	Cu	Ni	Mo	Al
CS	0.065	0.05	1.54	0.013	0.001	0.25	0.04	0.04	0.007	0.041

The corrosion experiments were conducted in a 7.5-liter autoclave (UNS N10276) which contained a CS working electrode, a HPHT Ag/AgCl reference electrode, a platinum-coated niobium counter electrode, and a HPHT ZrO₂-based pH electrode. A schematic of the experimental setup is shown in Figure 1. The test solution was a 1 wt.% NaCl aqueous electrolyte prepared using DI water. An impeller was used to stir the solution and to generate flow velocities of about 1 m/s and 1.7 m/s (1000 rpm and 1700 rpm, respectively) during the tests.

The experimental procedure is outlined in Figure 2. Initially, 6 liters of 1 wt.% NaCl solution was placed in the autoclave and purged with a high flow rate of CO₂ for 1 ~ 3 hours in order to remove dissolved O₂. The specimens were then placed in the autoclave while purging with CO₂ to avoid air ingress. After closing the autoclave, additional purging with CO₂ or a mixture of CO₂/10% H₂S was performed for 1 to 2 hours to ensure the removal of O₂ and the saturation of CO₂ or CO₂/H₂S, and then the temperature was increased to the testing temperature. Once the working temperature was reached, the working H₂S partial pressure was achieved by pressurizing with a mixture of CO₂/10% H₂S for the CO₂/H₂S conditions. High pressure was then attained by injecting CO₂ with a booster pump.

⁽¹⁾ UNS numbers are listed in Metals and Alloys in the Unified Numbering System, published by the Society of Automotive Engineers (SAE International) and cosponsored by ASTM International.

Corrosion rate and corrosion potential of specimens were evaluated with time by linear polarization resistance (LPR) measurements. The corrosion rates were also determined from the weight-loss (WL) method at the end of the test. The details of LPR and WL measurements are shown in previous studies.^{22,23} The solution pH was measured at the beginning and end of the experiment by using a commercial HPHT ZrO₂-based pH electrode and the HPHT Ag/AgCl reference electrode. The electrodes were calibrated prior to each test by the procedure supplied by the manufacturer.²⁴ After each test, the morphology and compositions of corrosion products were analyzed with scanning electron microscopy (SEM), energy-dispersive X-ray spectroscopy (EDS), and X-ray diffraction (XRD). Table 2 shows the test conditions for the present study.

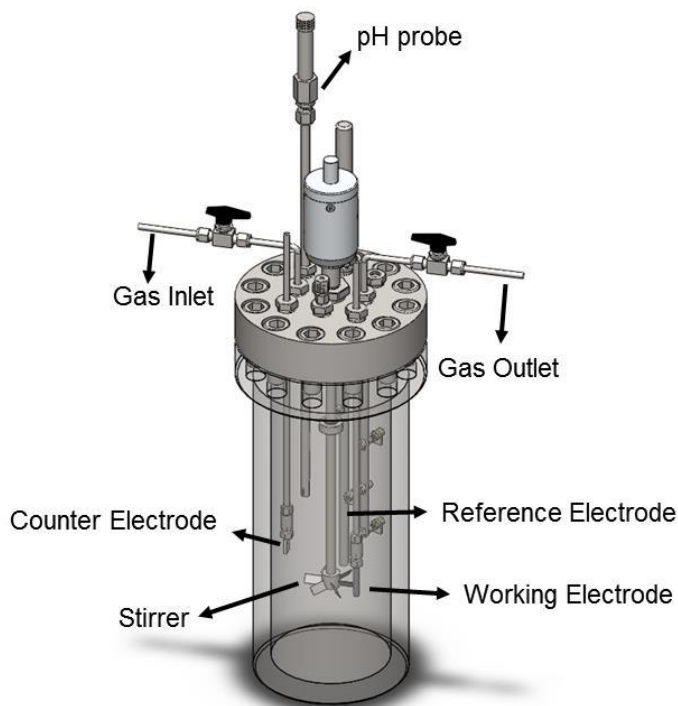


Figure 1: Schematic diagram of the autoclave used for the test under HPHT condition.

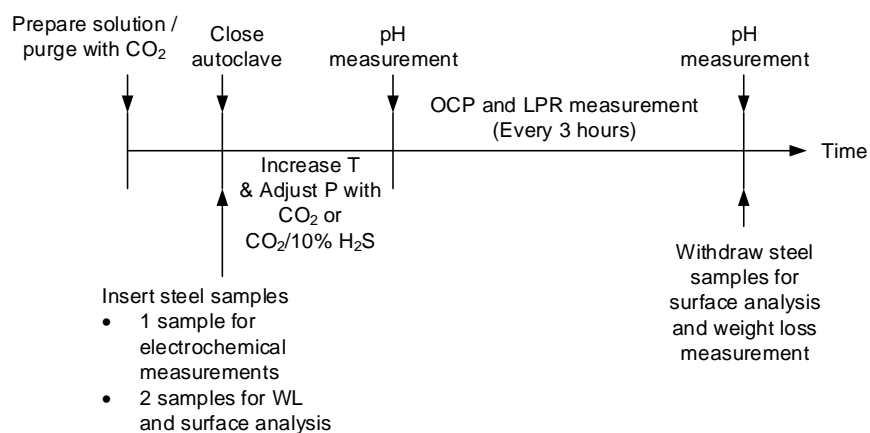


Figure 2: Experimental procedures for evaluating the corrosion behavior in HPHT CO₂ environments with H₂S.

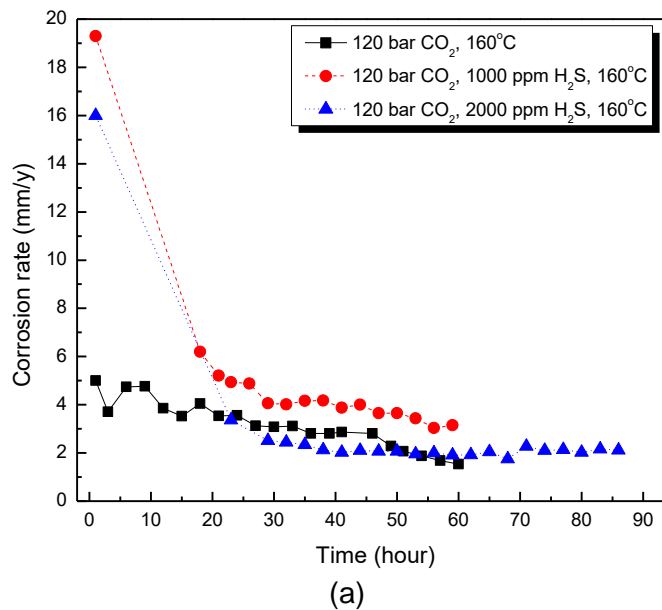
Table 2
Test conditions for corrosion testing

	pCO ₂ (MPa)	H ₂ S (ppm _v)	Temperature (°C)	Rotation speed (rpm)
1	12	0	160	1000
2	12	1000	160	1000
3	12	2000	160	1000
4	12	2000	160	1700

RESULTS AND DISCUSSION

Figure 3 shows LPR and weight loss (WL) corrosion rate data of CS exposed to 1 wt.% NaCl at 12 MPa CO₂ and 160°C with 0, 1000 and 2000 ppm H₂S. The corrosion rate of CS for the CO₂ condition was about 5 mm/y at the beginning of the experiment and then slightly decreased with time, whereas the corrosion rates of CS with H₂S (for both H₂S concentrations) started at much higher values and then decreased to similar values to those of the CO₂ condition after 20 hours. WL corrosion rate shows the same trend as the LPR corrosion rate.

Table 3 lists the solution pH values at the beginning and the end of each test. For all three conditions, the solution pH slightly increased indicating a small change in the bulk water chemistry due to the release of Fe²⁺.



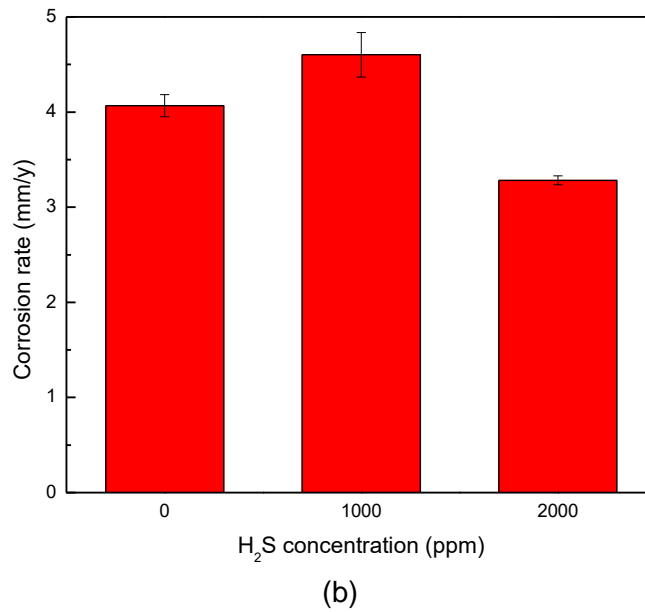


Figure 3: Comparison of corrosion rate with different H₂S concentrations at 12 MPa CO₂ and 160°C: (a) LPR corrosion rate, (b) WL corrosion rate.

**Table 3
Measured initial and final solution pH at 12 MPa CO₂ and 160°C.**

	Initial pH	Final pH
0 ppm H ₂ S	4.3	4.8
1000 ppm H ₂ S	4.2	4.7
2000 ppm H ₂ S	4.4	4.8

Figure 4 shows the surface morphology and chemical analysis of the corroded sample after 60 hours of exposure to the CO₂ condition. A uniform corrosion product was found covering the exposed surface. EDS analysis shows that the corrosion product mainly consists of iron, carbon, and oxygen.

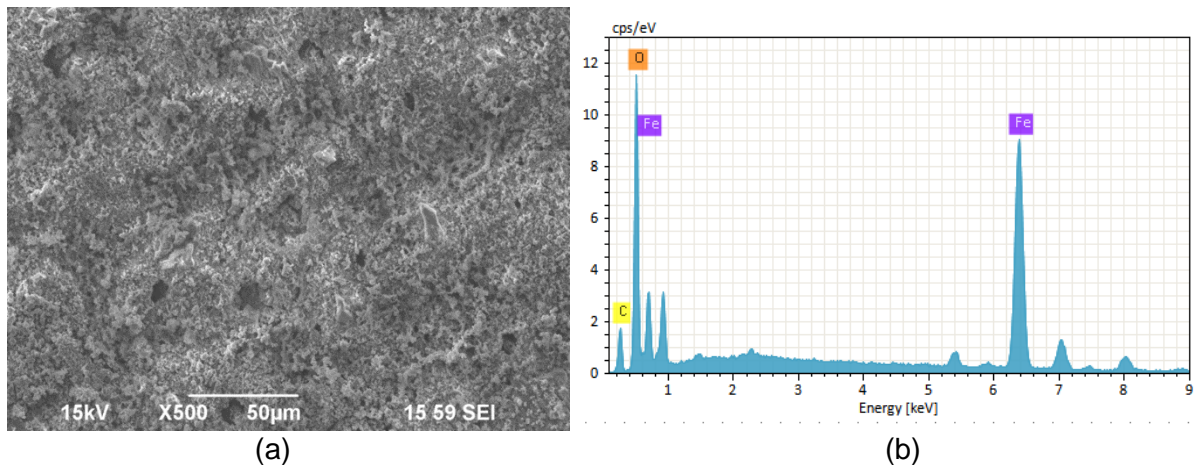


Figure 4: SEM surface view (a) and EDS analysis (b) of the corrosion product formed at 12 MPa and 160°C.

Figure 5 shows cross-sectional SEM images of the corroded sample exposed to the CO₂ condition. It can be seen that most of the surface was covered by a thick corrosion product layer (~ 30 μm). However, there are several areas where the corrosion product layer is thinner (~ 5 μm, Figure 5 (b)).

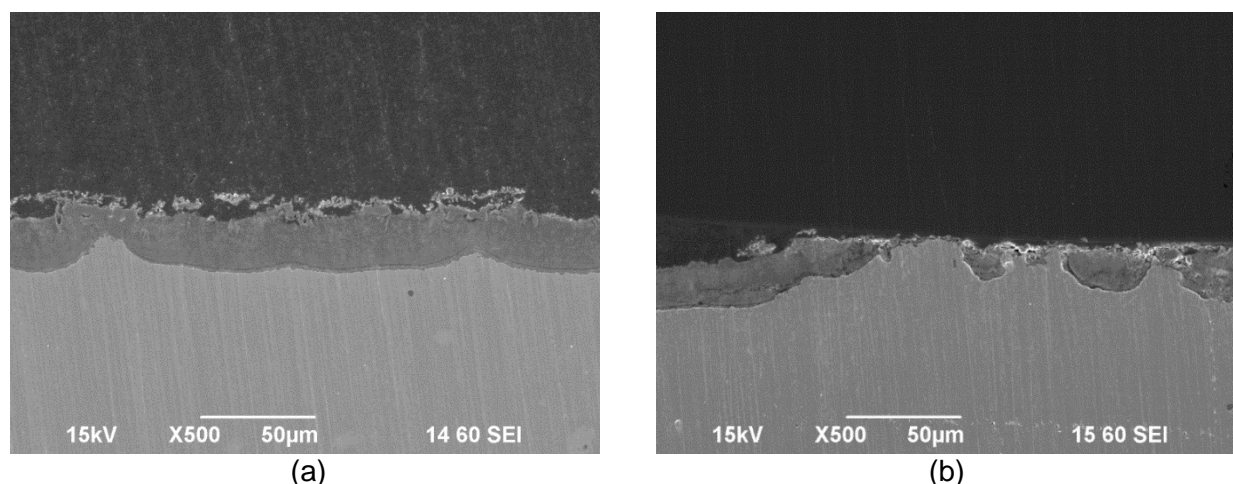


Figure 5: SEM cross-sectional view of the corroded sample at 12 MPa CO₂ and 160°C.

In order to identify the compositions of the corrosion product layer and their distribution, cross-sectional EDS mapping analysis was conducted (Figure 6). It shows that the thick compact layer is rich in iron (blue mapping), carbon (red mapping), and oxygen (green mapping). Scattered particles are found above the thick layer, which contains higher relative oxygen content than the thick layer.

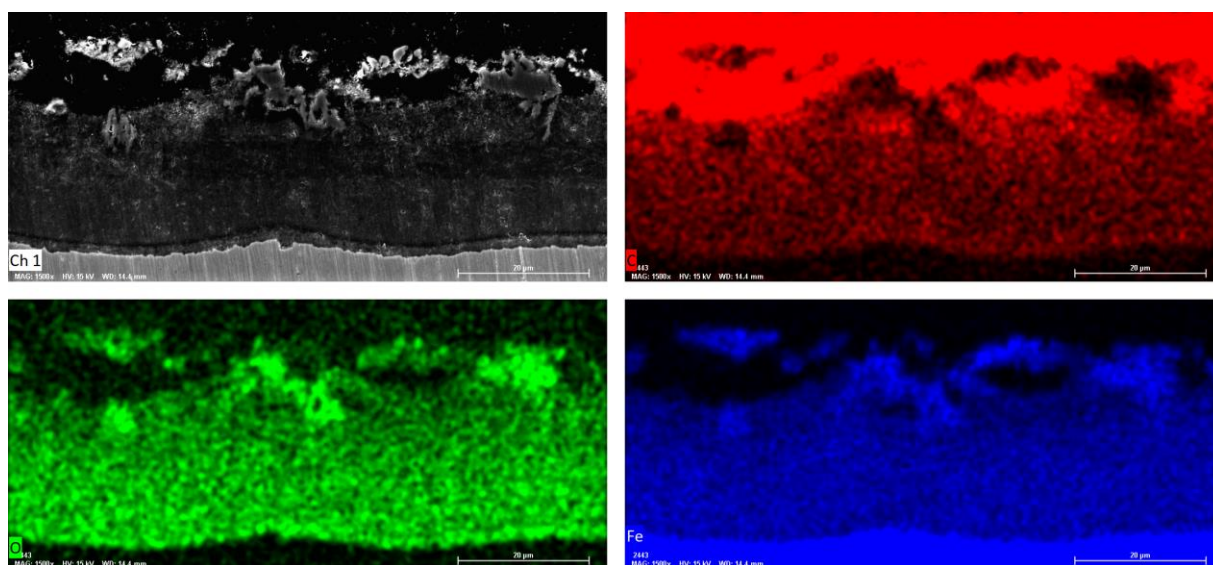


Figure 6: SEM and EDS elemental mapping images of the cross-section of the corrosion product layer produced after 60 hours of exposure in 12 MPa CO₂ and 160°C.

Figure 7 shows the XRD pattern of the corrosion product layer formed at 12 MPa CO₂ and 160°C. The layer formed in this condition showed dominant FeCO₃ diffraction patterns with some Fe₃O₄. Based on the EDS mapping (Figure 6) and XRD results (Figure 7), it is identified that the thick layer is FeCO₃ and that some Fe₃O₄ is present possibly on top of the FeCO₃ layer. This indicates that FeCO₃ is a more favored corrosion product than Fe₃O₄ under the current experimental condition (12 MPa CO₂ and 160°C). The observations also suggest that the relatively high corrosion rate (> 1 mm/y) is attributed to the formation of only FeCO₃, which is less protective than Fe₃O₄.^{17,18,25}

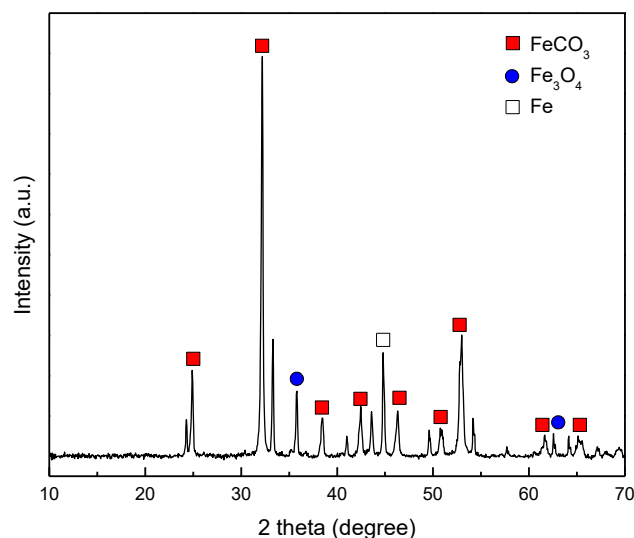


Figure 7: XRD surface analysis of the CS sample exposed to 12 MPa CO₂ at 160°C.

Figure 8 shows the surface morphology and chemical analysis of the corrosion product formed at 12 MPa CO₂ and 160°C with 1000 ppm H₂S. A uniform corrosion product was found covering the exposed surface. In this case, EDS analysis shows that the corrosion product mainly consists of iron and sulfur.

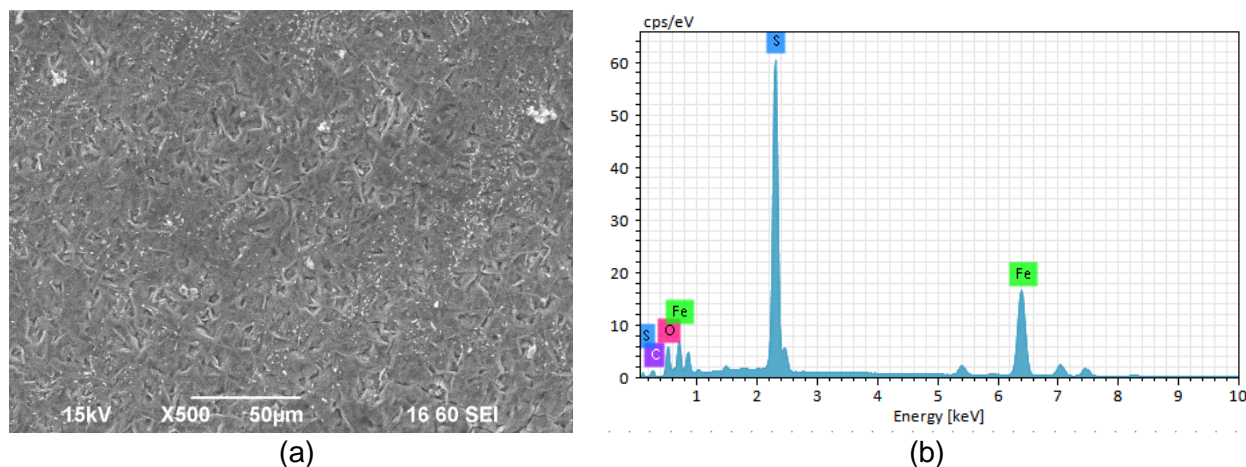
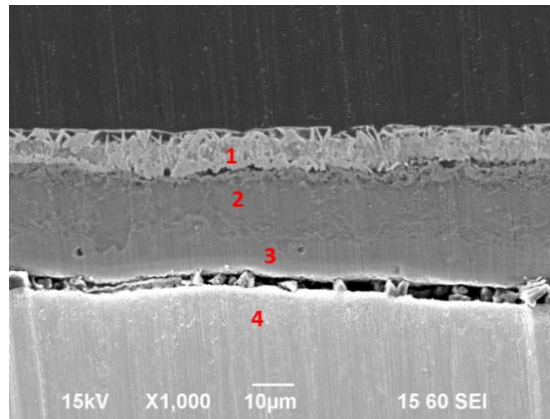


Figure 8: SEM surface view (a) and EDS analysis (b) of the corrosion product formed at 12 MPa CO₂ and 160°C with 1000 ppm H₂S.

Figure 9 represents the cross-sectional morphologies and chemical analysis of the corrosion product formed at 12 MPa CO₂ and 160°C with 1000 ppm H₂S. It can be seen that it has a two-layer structure; a thin outer Fe and S containing layer and a thick/continuous inner Fe, C and O containing layer. This was also confirmed by the results of the EDS line scanning analysis (Figure 10) and mapping analysis (Figure 11). It is worth noting that there is a gap between the steel surface and the corrosion product, possibly due to the poor adhesion of the inner layer to the substrate. This can consequently reduce the protectiveness of the corrosion product layer and increase the corrosion rate.²³



At.%	C	O	S	Fe
1	36.18	1.20	30.39	29.99
2	42.96	28.47	2.49	25.56
3	25.90	36.78	4.49	32.46
4	13.52	-	-	86.48

Figure 9: Cross-sectional SEM and EDS analysis of the corrosion product formed at 12 MPa and 160°C with 1000 ppm H₂S.

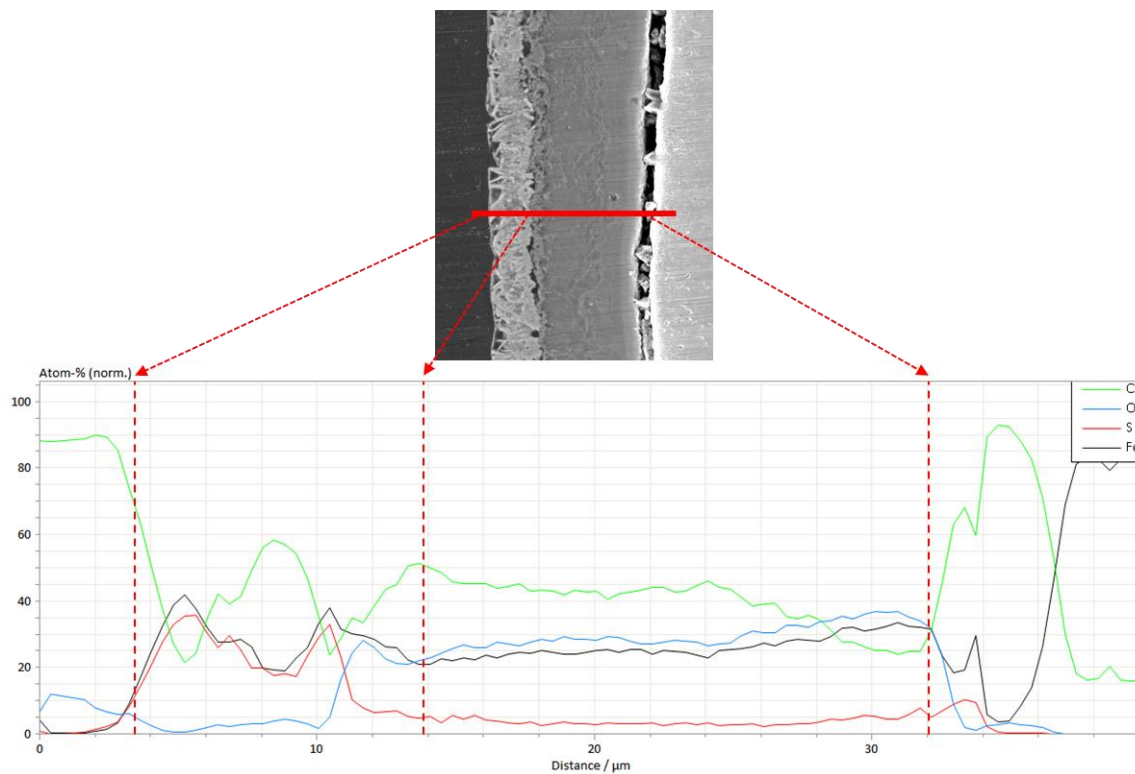


Figure 10: Cross-sectional EDS line scanning of the corrosion product formed at 12 MPa CO₂ and 160°C with 1000 ppm H₂S.

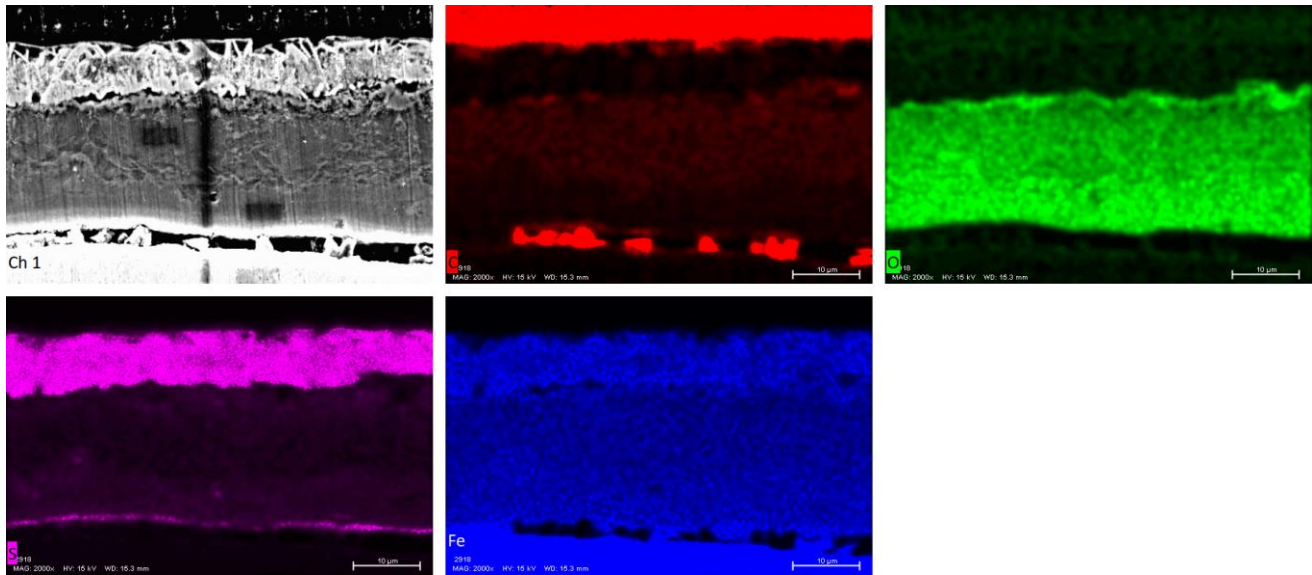


Figure 11: Cross-sectional SEM and EDS elemental mapping of the corrosion product formed at 12 MPa CO₂ and 160°C with 1000 ppm H₂S.

Figure 12 shows the surface morphology and chemical analysis of the corrosion product formed at 12 MPa CO₂ and 160°C with 2000 ppm H₂S. Similar to the case with 1000 ppm H₂S, a uniform corrosion product was found covering the exposed surface. EDS analysis shows that the corrosion product mainly consists of iron and sulfur. Small amounts of carbon and oxygen are also detected.

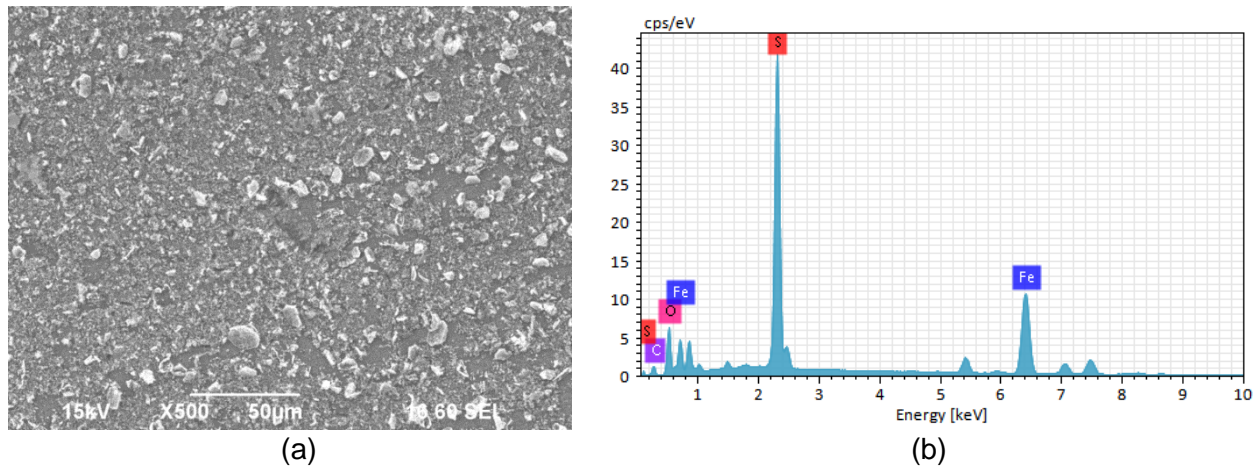
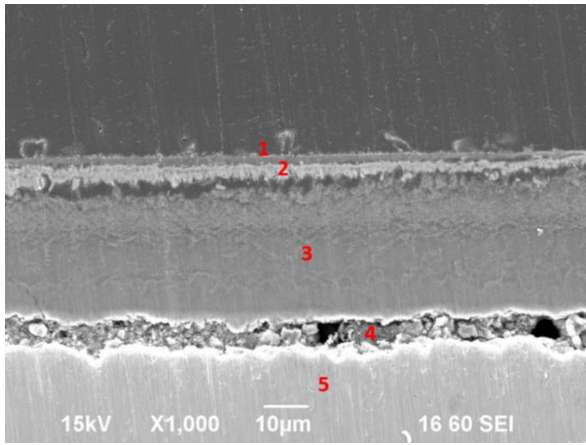


Figure 12: SEM surface view (a) and EDS analysis (b) of the corrosion product formed at 12 MPa CO₂ and 160°C with 2000 ppm H₂S.

Figure 13 to Figure 15 represent the cross-sectional EDS analysis (point, line scanning and mapping) of the corrosion product formed at 12 MPa CO₂ and 160°C with 2000 ppm H₂S. As in the previous case with 1000 ppm H₂S, the corrosion product has a two-layer structure; a thin outer Fe and S containing layer and a thick/continuous inner Fe, C and O containing layer. Furthermore, a gap is also found between the inner layer and the metal surface due to the undermining effect of the corrosion process.



At.%	C	O	S	Fe
1	66.76	6.74	13.04	8.04
2	27.85	0.63	35.81	34.73
3	49.06	21.89	4.70	23.64
4	27.10	10.80	23.44	37.52
5	18.40	-	-	81.60

Figure 13: Cross-sectional EDS analysis of the corrosion product formed at 12 MPa CO₂ and 160°C.

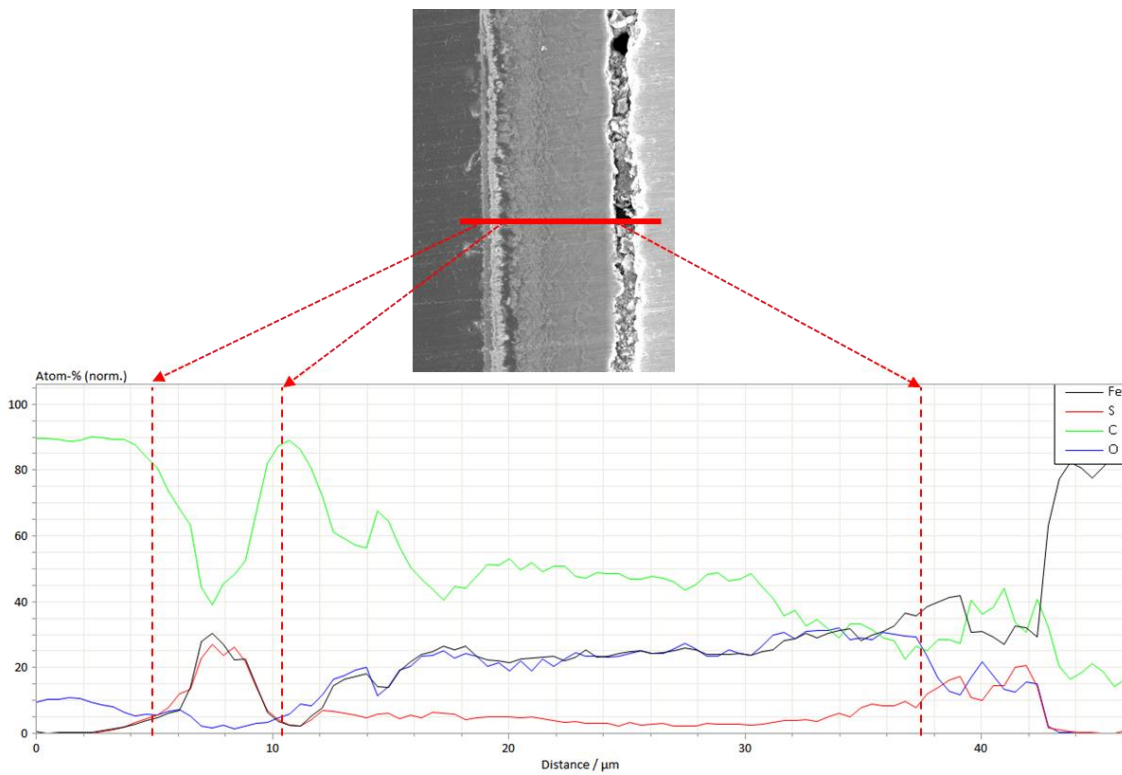


Figure 14: Cross-sectional EDS line scanning of the corrosion product formed at 120 MPa CO₂ and 160°C with 2000 ppm H₂S.

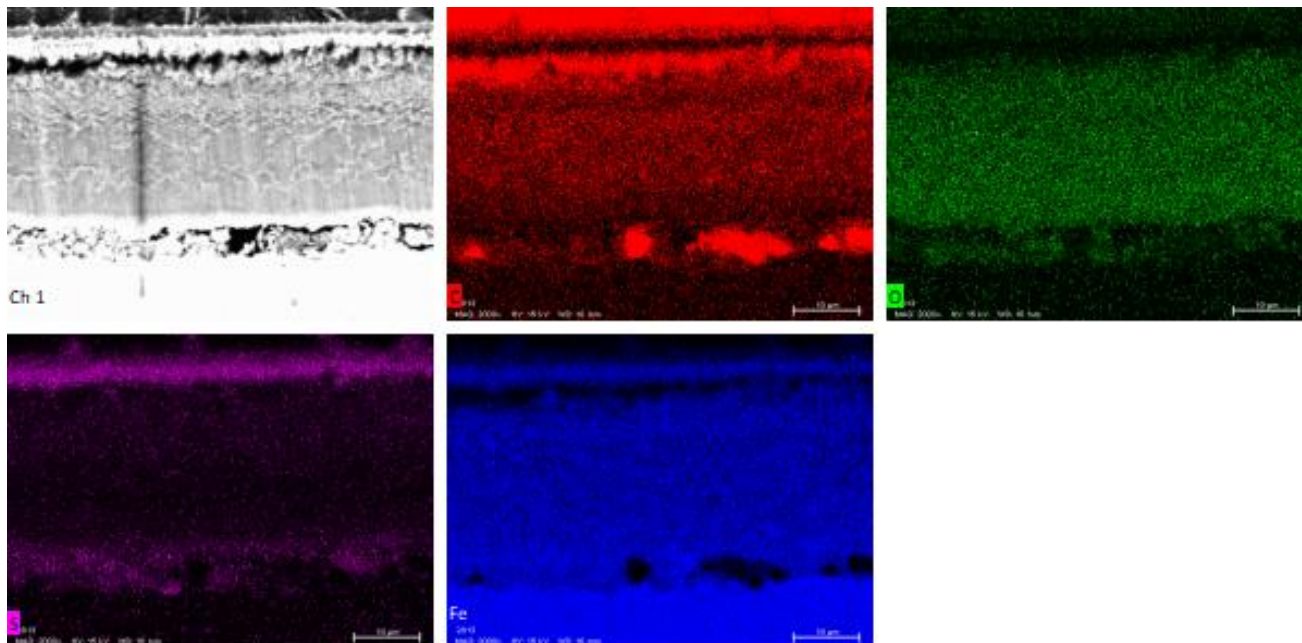


Figure 15: Cross-sectional SEM and EDS elemental mapping of the corrosion product formed at 12 MPa CO₂ and 160°C with 2000 ppm H₂S.

Figure 16 shows the XRD pattern of the corrosion product layer formed at 12 MPa CO₂ and 160°C with 2000 ppm H₂S. The layer formed in this condition showed FeCO₃ diffraction patterns with pyrrhotite (Fe_{1-x}S). This allowed ready identification of the corrosion products formed in CO₂/H₂S conditions as Fe_{1-x}S for the outer layer and FeCO₃ for the inner layer. It is interesting to note that Fe₃O₄ was not detected in the corrosion products formed in CO₂/H₂S conditions and the predominant corrosion product was FeCO₃, the same as the CO₂ condition.

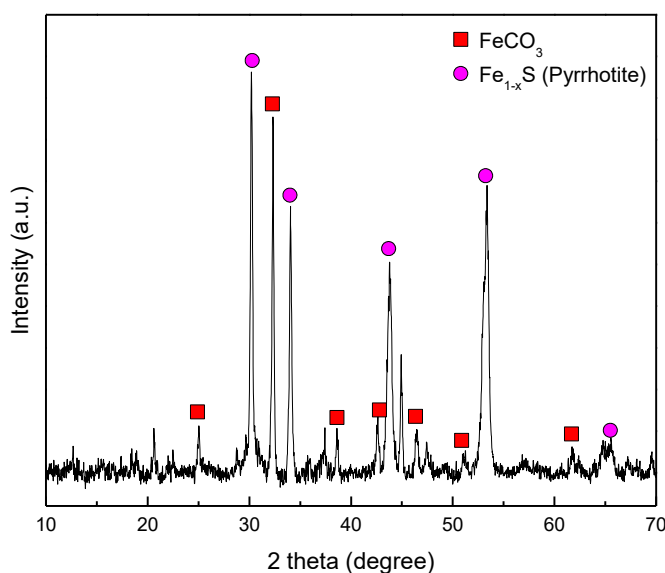


Figure 16: XRD surface analysis of the CS sample exposed to 2000 ppm H₂S and 12 MPa CO₂ at 160°C.

It has been reported that thin and continuous Fe₃O₄ layer formed at steel surface provides instantaneous corrosion protection at high temperatures (> 120°C).^{17,25,26} Although the increase in CO₂ partial pressure makes the formation of FeCO₃ more favorable compare to Fe₃O₄, Fe₃O₄ coexists with FeCO₃ and offers

corrosion protection.¹⁸ However, in the present study, relatively high corrosion rate (> 1 mm/y) was measured with very high CO_2 partial pressure (12 MPa), and the corrosion behavior was controlled by a thick FeCO_3 layer. Furthermore, subsequent formation of an outer Fe_{1-x}S layer provided no additional corrosion protection. It can be speculated that increased concentration of CO_2 species in aqueous environment could affect the thermodynamic stability and kinetics of Fe_3O_4 formation. Further work is required to examine the relationship of the CO_2 partial pressure with the formation of Fe_3O_4 at high temperatures.

In order to evaluate the effect of flow velocity on the corrosion behavior of CS at 160°C , an autoclave test was conducted at higher rotation speed of 1700 rpm. A comparison of the corrosion rates with different rotation speeds (1000 rpm and 1700 rpm) at 12 MPa CO_2 and 160°C with 2000 ppm H_2S is shown in Figure 17. For both cases, the corrosion rate decreased with time and slightly higher corrosion rate was measured for the case with 1700 rpm compared with 1000 rpm. The morphology and composition of the corrosion product were almost identical with the 1000 rpm case (Figure 18) indicating that the corrosion behavior of CS in the $\text{CO}_2/\text{H}_2\text{S}$ condition does not vary within the tested flow velocities. This also implies that the surface water chemistry is supersaturated with respect to FeCO_3 even in conditions where mass transfer is accelerated by flow.^{17,27}

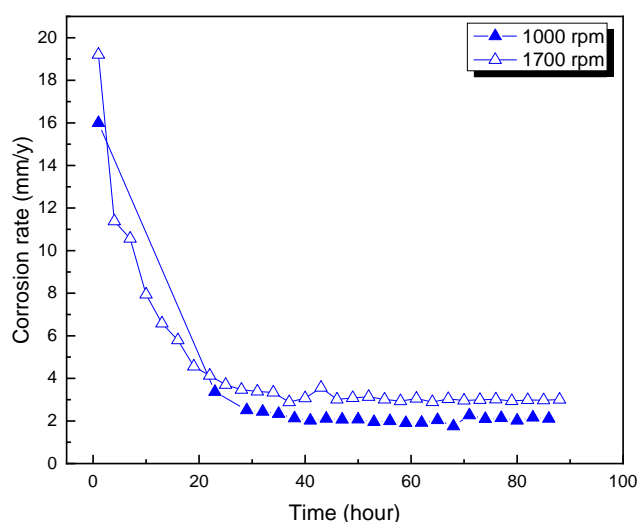


Figure 17: Comparison of corrosion rates of CS with different rotation speed of impeller at 12 MPa CO_2 and 160°C with 2000 ppm H_2S .

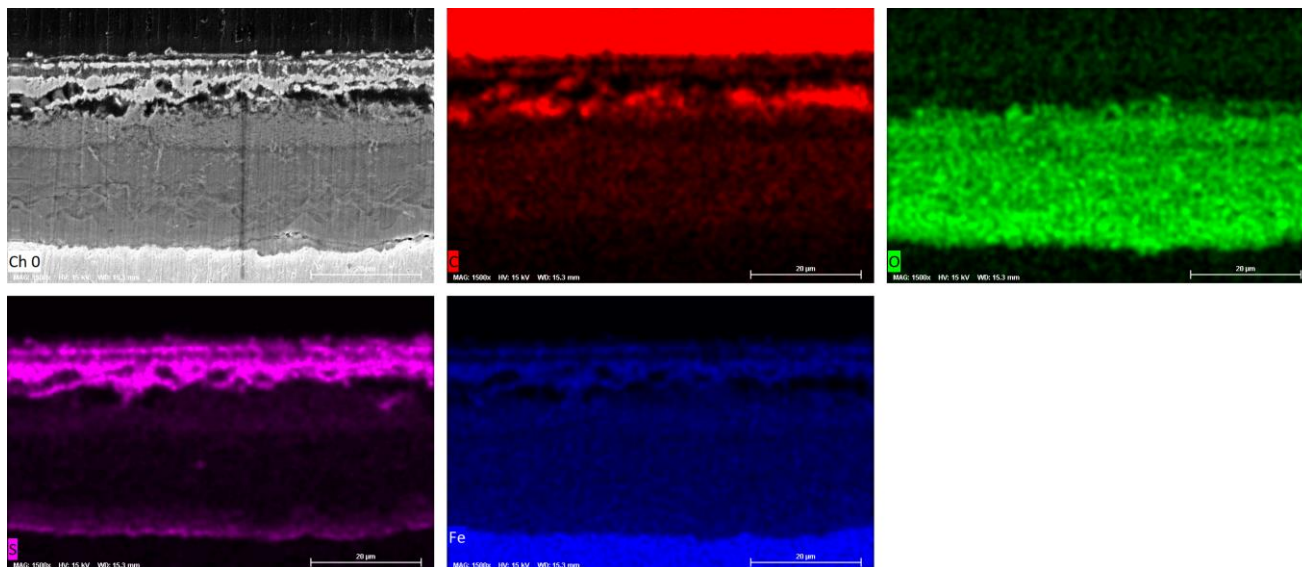


Figure 18: Cross-sectional SEM and EDS elemental mapping of the corrosion product formed at 12 MPa CO₂ and 160°C with 2000 ppm H₂S (1700 rpm).

CONCLUSIONS

The effect of H₂S on the aqueous corrosion behavior of CS was evaluated at high pressure (12 MPa) and high temperature (160°C) in supercritical CO₂ conditions. The following conclusions are drawn:

- No significant difference in the corrosion rate in the presence of H₂S was observed.
- The predominant corrosion product was FeCO₃ for all conditions, indicating that the formation of FeCO₃ is more favorable than that of FeS and Fe₃O₄ at these conditions.
- No significant effect of flow velocity was observed on the corrosion behavior of CS.

REFERENCES

1. J. Veron, "An Overview of the Non-Developed Gas Reserves in Southeast Asia," *PetroMin* (2007): p. 22.
2. T.E. Perez, "Corrosion in the Oil and Gas Industry: An Increasing Challenge for Materials," *JOM* 65 (2013): p. 1033.
3. J. Carew, A. Al-Sayegh, A. Al-Hashem, "The Effect of Water-Cut on the Corrosion Behavior L80 Carbon Steel Under Downhole Conditions," CORROSION/2000, paper no. 00061 (Houston, TX: NACE, 2000).
4. J. Carew, A. Al-Hashem, "CO₂ Corrosion of L-80 Steel in Simulated Oil Well Conditions," CORROSION/2002, paper no. 02299 (Houston, TX: NACE, 2002).
5. M.B. Kermani, J.C. Gonzales, G.L. Turconi, D. Edmonds, G. Dicken, L. Scoppio, "Development of Superior Corrosion Resistance 3%Cr Steels for Downhole Applications," CORROSION 2003, paper no. 03116 (Houston, TX: NACE, 2003).
6. A. Al-Hashem, J. Carew, "Downhole Materials Optimization for Harsh Petroleum Production," CORROSION 2003, paper no. 03346 (Houston, TX: NACE, 2003).
7. H.J. Choi, N.S. Al-Bannai, F.I. Al-Beheiri, "Field Corrosion Assessment of L80 Carbon Steel Downhole Production Tubing in Khuff Gas Wells," CORROSION 2006, paper no. 06653 (Houston, TX: NACE, 2006).
8. Y.S. Choi, F. Farelas, S. Nestic, A.A.O. Magalhães, C. de Azevedo Andrade, "Corrosion Behavior of Deep Water Oil Production Tubing Material under Supercritical CO₂ Environment: Part I. Effect of Pressure and Temperature," CORROSION 2013, paper no. 2380 (Houston, TX: NACE, 2013).

9. S. Sim, I. S. Cole, Y.S. Choi, N. Birbilis, "A Review of the Protection Strategies against Internal Corrosion for the Safe Transport of Supercritical CO₂ via Steel Pipelines for CCS Purposes," *International Journal of Greenhouse Gas Control* 29 (2014): p. 185.
10. L. Wei, Y. Zhang, X. Pang, K. Gao, "Corrosion Behaviors of Steels under Supercritical CO₂ Conditions," *Corrosion Reviews* 33 (2015): p. 151.
11. S. Sarrade, D. Feron, F. Rouillard, S. Perrin, R. Robin, J.C. Ruiz, H.A. Turc, "Overview on Corrosion in Supercritical Fluids," *Journal of Supercritical Fluids* 120 (2017): p. 335.
12. Y. Xiang, M. Xu, Y.S. Choi, "State-of-the-Art Overview of Pipeline Steel Corrosion in Impure Dense CO₂ for CCS Transportation: Mechanisms and Models," *Corrosion Engineering, Science and Technology* 52 (2017): 485.
13. R. Barker, Y. Hua, A. Neville, "Internal Corrosion of Carbon Steel Pipelines for Dense-Phase CO₂ Transport in Carbon Capture and Storage (CCS) - A Review," *International Materials Reviews* 62 (2017): p. 1.
14. Y. Zhang, X. Pang, S. Qu, X. Li, K. Gao, "Discussion of the CO₂ Corrosion Mechanism Between Low Partial Pressure and Supercritical Condition," *Corrosion Science* 59 (2012): p. 186.
15. J. Wang, L. Meng, Z. Fan, Q. Liu, Z. Tong, "Mechanism and Modelling of CO₂ Corrosion on Downhole Tools," *R. Soc. open sci.* 6 (2019): 181899.
16. H. Li, D. Li, L. Zhang, Y. Bai, Y. Wang, M. Lu, "Fundamental Aspects of the Corrosion of N80 Steel in a Formation Water System under High CO₂ Partial Pressure at 100°C," *RSC Adv.* 9 (2019): p. 11641.
17. T. Tanupabrungsun, "Thermodynamics and Kinetics of Carbon Dioxide Corrosion of Mild Steel at Elevated Temperatures," Ph.D. thesis, (Ohio University, 2012).
18. Y. Hua, S. Xu, Y. Wang, W. Taleb, J. Sun, L. Zhang, R. Barker, A. Neville, "The Formation of FeCO₃ and Fe₃O₄ on Carbon Steel and Their Protective Capabilities against CO₂ Corrosion at Elevated Temperature and Pressure," *Corrosion Science* 157 (2019): p. 392.
19. S. Gao, P. Jin, B. Brown, D. Young, S. Netic, M. Singer, "Effect of High Temperature on the Aqueous H₂S Corrosion of Mild Steel," *Corrosion* 73 (2017): p. 1188.
20. S. Gao, B. Brown, D. Young, S. Netic, M. Singer, "Formation Mechanisms of Iron Oxide and Iron Sulfide at High Temperature in Aqueous H₂S Corrosion Environment," *Journal of the Electrochemical Society* 165 (2018): p. C171.
21. S. Gao, B. Brown, D. Young, M. Singer, "Formation of Iron Oxide and Iron Sulfide at High Temperature and Their Effects on Corrosion," *Corrosion Science* 135 (2018): p. 167.
22. Y.S. Choi, S. Hassani, T.N. Vu, S. Netic, A.Z.B. Abas, A.M. Nor, M.F. Suhor, "Corrosion Inhibition of Pipeline Steels under Supercritical CO₂ Environment," CORROSION 2017, paper no. 9153 (Houston, TX: NACE, 2017).
23. Y.S. Choi, S. Hassani, T.N. Vu, S. Netic, A.Z.B. Abas, "Effect of H₂S on the Corrosion Behavior of Pipeline Steels in Supercritical and Liquid CO₂ Environments," *Corrosion* 72 (2016): p. 999.
24. "High Temp & High Pressure pH Electrode", Corr Instrumnets, www.corrinstruments.com.
25. T. Tanupabrungsun, D. Young, B. Brown and S. Netic, "Construction and Verification of Pourbaix Diagrams for CO₂ Corrosion of Mild Steel Valid up to 250°C," CORROSION 2012, paper no. 0001418 (Houston, TX: NACE, 2012).
26. N. Mundhenk, S. Carrero, K.G. Knauss, R. Wonneberger, A. Undisz, Y. Wu, "Kinetic and Thermodynamic Analysis of High-Temperature CO₂ Corrosion of Carbon steel in Simulated Geothermal NaCl Fluids," *Corrosion Science* 171 (2020): p. 108597.
27. S. Netic, G. T. Solvi, J. Enerhaug, "Comparison of the Rotating Cylinder and Pipe Flow Tests for Flow-Sensitive Carbon Dioxide Corrosion," *Corrosion* 51 (1995): p. 773.